Available online at www.sciencedirect.com

ScienceDirect

Underground Space 26 (2026) 106–125

www.keaipublishing.com/undsp

Research Paper

Physical model test and numerical simulation for the interaction analysis between tunnel and masonry arch bridge

Si-Yi Huang [a], Li-Yuan Tong [a,*], Ming-Fei Zhang [b], Tao Qiu [a], Xiao-Dong Li [c], Jia-Jia Wan [d]

[a] School of Transportation, Southeast University, Nanjing 211189, China
[b] Civil Engineering and Architecture Institute, Zhengzhou University of Aeronautics, Zhengzhou 450046, China
[c] Nanjing Metro Construction Co., Nanjing 210000, China
[d] Beijing Urban Construction Zhongnan Civil Engineering Group Co., Ltd., Beijing 100124, China

Received 15 December 2024; received in revised form 28 July 2025; accepted 31 July 2025
Available online 13 November 2025

Abstract

Masonry arch bridges serve as essential transport infrastructure and are often protected as cultural heritage sites. While most studies emphasize their response to vertical loading, limited attention has been given to their behavior under the influence of nearby tunnel excavation. This study investigates the interaction between tunnel-induced ground movement and masonry arch bridges through physical model tests and numerical simulations. Two typical arch bridge types are examined to assess deformation patterns caused by tunneling. A coupled discrete element and finite difference method is proposed to simulate soil–structure interactions, and the model is validated against experimental results. The results highlight that the arch span has a major impact on soil behavior. Larger spans lead to wider settlement zones and more uniform stress distribution but increase structural vulnerability. Semi-circular arches develop tensile strain at the crown and compressive strain at the foot under tunneling. Meanwhile, the joint displacements follow a three-dimensional Gaussian distribution, influenced by tunnel volume loss and burial depth, especially in circular arches. Increasing Young's modulus and joint shear stiffness of masonry arch bridges through technical means, such as grouting, is helpful to reduce deformation and cracking. These findings support risk assessment and design improvements for masonry bridges in tunneling environments.

Keywords: Physical model test; Numerical simulation; Masonry arch bridge; Soil-structure interaction; DEM–FDM

1 Introduction

In response to urban growth and increased mobility demands, many cities have expanded underground spaces and transport infrastructure to improve living conditions (Broere, 2016; Cui & Nelson, 2019). While underground rail systems enhance connectivity, their construction can negatively affect nearby structures, raising concerns among urban planners (Liang et al., 2016; Lin et al., 2024; Sirivachiraporn & Phienwej, 2012). As interest in preserving historical architecture grows, masonry arch bridges have become a focus of protection efforts.

Masonry arches possess strong load-bearing capacity and structural stability due to their curved geometry (Sarhosis et al., 2016). However, these structures are typically constructed from stone or brick masonry, which have high rigidity but low toughness, making them less adaptable to foundation settlement and external forces. In soft soil regions, tunnel excavation often causes foundation settlement and stress concentration, which can result in cracking, displacement, or local collapse of these structures (Bilotta et al., 2017; Chiu et al., 2014; Zhang et al., 2024).

Extensive research has addressed the mechanical behavior and failure mechanisms of masonry arch structures. Milani and Lourenço (2012) proposed a three-

* Corresponding author.
E-mail address: 101010519@seu.edu.cn (L.-Y. Tong).
Peer review under the responsibility of Tongji University

https://doi.org/10.1016/j.undsp.2025.07.006

dimensional discrete element model to analyze the static nonlinear response of full-scale masonry arch bridges, confirming its validity through case studies. Forgács et al. (2018) applied the discrete element method to assess how various construction schemes influence the load-bearing behavior of single-span tilted arches, identifying three main failure modes: pure rotational mechanism, mixed failure, and failure of the unsupported acute-angled corner. In parallel, physical model testing has proven effective in evaluating damage patterns and structural performance in masonry arches (Augusthus-Nelson & Swift, 2020; Augusthus-Nelson et al., 2018; Liu et al., 2024; Sarhosis et al., 2024).

In the context of tunnel–masonry interaction, Amorosi (2014) used a two-dimensional geotechnical–structural finite element model to investigate deformation and cracking in historic masonry due to shallow tunneling, using Rome's Felice aqueduct as a case study. The coupled model outperformed free-field predictions in accuracy. Yiu et al. (2017) developed a three-dimensional model of a typical London soil profile to examine the effects of single and twin tunnels beneath masonry buildings with bar foundations. The results showed that reliable damage predictions can be obtained by modeling critical components, such as masonry walls and foundations, without representing the entire superstructure.

The finite difference method (FDM) is widely adopted in geotechnical and structural analysis, yet finite element methods often struggle to capture discontinuities in masonry without a complex contact model. As a result, deformation predictions using traditional finite element or damage models tend to be overly conservative. In contrast, the discrete element method (DEM) effectively models fracture and joint behavior in masonry but becomes computationally intensive when applied to large continuous domains like the surrounding soil.

To overcome these limitations, this study proposes a coupled discrete element–finite difference modeling approach. In this framework, DEM captures the nonlinear fracture and contact behavior of masonry arch components, while FDM efficiently simulates the continuous response of the surrounding soil. This integrated method offers a balanced solution between computational efficiency and modeling accuracy, providing a more realistic tool for analyzing tunnel-induced effects on masonry bridges.

Complementing the numerical approach, physical model tests were conducted using an advanced photogrammetric monitoring system to record displacements of both the arch bridge and surrounding soil. This non-contact technique minimizes interference with the physical model while enabling real-time, high-resolution measurement of deformation and stress distributions (Borlenghi et al., 2023; Conde et al., 2017; Sun et al., 2022). The reliability of the coupled numerical models was verified through comparison with experimental results. Together, the combined use of high-fidelity physical monitoring and coupled numerical modeling offers a robust framework for predicting the structural response of masonry bridges to tunnel excavation and supports practical applications in urban underground construction.

2 Overview of model test

2.1 Model test systems and monitoring scheme

In this study, a physical model test was conducted to simulate the tunnel excavation process beneath masonry arch bridges supported by either separate footings or spread foundations. The experimental setup consisted of a model box, a tunnel model, masonry bridge models, and a data acquisition system, as shown in Fig. 1(a). The model box, made of transparent acrylic panels, was designed to ensure both structural integrity and ease of assembly. To minimize boundary effects and ensure sufficient soil domain for analysis, the box dimensions were set as 1.0 m in length, 1.0 m in height, and 0.2 m in width. For the purposes of the experiment, the box was assumed to behave as a rigid boundary.

The primary focus was to evaluate the influence of tunnel-induced strata volume loss on the surrounding soil and adjacent structures. A high-stiffness PVC pipe with an outer diameter of 140 mm was used to represent the tunnel lining (Fig. 1(b)). To simulate ground loss during shield tunneling, the tunnel was wrapped in a rubber membrane and volume loss was controlled by extracting fluid from the membrane, following the method proposed by Ng et al. (2013) and Wang et al. (2020).

Masonry arch bridges are known for their structural stability and are commonly built using stone or concrete blocks. Among the common designs, the semicircular and circular arches are widely adopted in practical engineering. In this study, scaled bridge models based on these two classical cross-sectional shapes were constructed, as shown in Fig. 1(c) and (d). The parametric equations defining the geometry of each arch type are provided below.

Semi-circular arch bridge :

$$\begin{cases} x = 9.6\cos\theta, \\ y = 9.6\sin\theta, \end{cases} \quad \theta \in \left(-\frac{\pi}{2}, \frac{\pi}{2}\right). \tag{1}$$

Circular arch bridge :

$$\begin{cases} x = 28.3\cos\theta, \\ y = -19.6 + 28.3\sin\theta, \end{cases} \quad \theta \in \left(-\frac{8}{15}\pi, \frac{8}{15}\pi\right). \tag{2}$$

Previous studies (Chen et al., 2016; Zhang et al., 2024) have shown that the Young's modulus and shear strength of masonry are the key factors affecting its deformation and failure behavior. In this study, the selected materials are designed to meet similarity requirements while remaining practical for fabrication. Gypsum is chosen as the main component for the masonry blocks, and a polycarboxylic acid-based water-reducing agent is added to

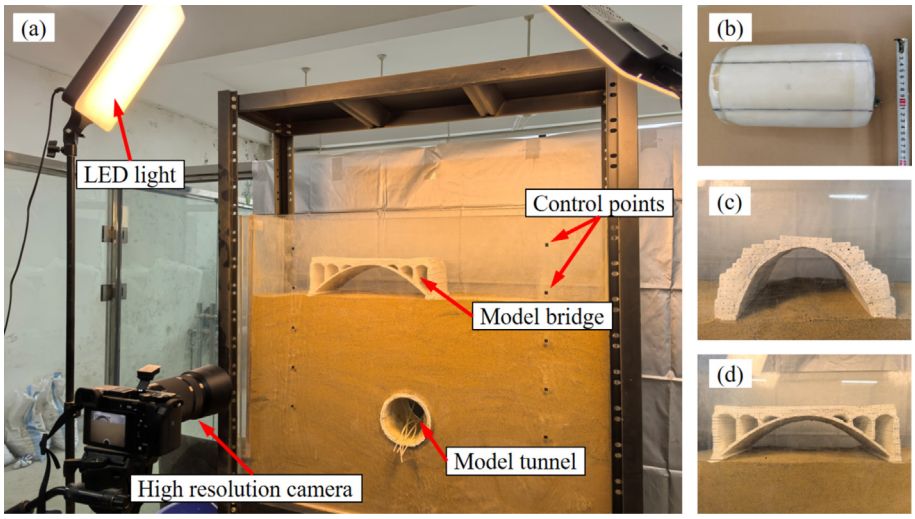

Fig. 1. Schematic of model test setup. (a) Distribution of testing equipment, (b) tunnel model, (c) semi-circular arch bridge model, and (d) circular arch bridge model.

ensure sufficient mechanical strength. Lime mortar is used to fill the joints between blocks, completing the assembly of the masonry arch bridge model.

The experimental monitoring system consists of a high-resolution camera (24.2 megapixels), LED floodlights, a data acquisition computer, and particle image velocimetry software (PIVlab). The image-based tracking system enables micrometer-scale resolution in capturing displacement and deformation fields (Stamhuis & Thielicke, 2014). This non-contact technology is particularly effective in monitoring soil surface settlement and structural displacement caused by tunnel volume loss. Its high accuracy and real-time capabilities support precise data collection and enhance the reliability of physical model analysis.

The primary objective of the physical model test is to investigate the deformation characteristics and load transfer mechanisms of existing masonry structures under tunnel excavation. To this end, a fine sand layer is used to simulate the surrounding soil, consistent with the geological conditions of the tunnel. The sand is sourced from river deposits along the Yangtze River in Nanjing, China. The particle size distribution of the sand used in the experiment is shown in Fig. 2.

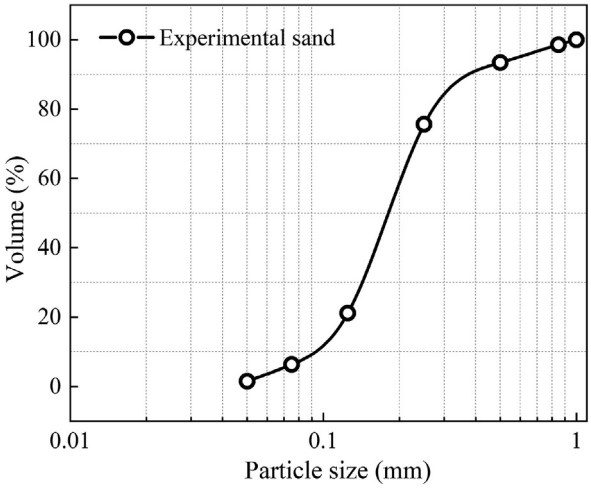

Fig. 2. Particle size distribution of experimental sand.

2.2 Similarity principles and analogous materials

To ensure that the behavior of the physical model accurately represents that of the prototype, the experiment must satisfy the fundamental principles of similarity, including geometric, material, and dynamic similarity. Based on the Buckingham π theorem, any physical problem involving n-dimensional variables and α fundamental dimensions can be reduced to a set of $(n-\alpha)$ dimensionless π terms. For the case of geotechnical-structural interaction problems under gravity, the key physical quantities governing the response of the system include geometric dimension l, unit weight γ, displacement δ, Young's modulus E, Poisson's ratio μ, cohesion c, friction angle φ, stress σ, and strain ε.

$$f(l,\gamma,\delta,E,\mu,c,\varphi,\sigma,\varepsilon)=0 \tag{3}$$

There were a total of nine parameters, which contained two basic physical dimensions (geometric dimension l and unit weight γ). According to the Buckingham π theorem (Gibbings, 2011; Wang et al., 2019), the key dimensionless π groups relevant to the current tunnel-soil-masonry interaction system are as follows:

$$\pi_1=\frac{\delta}{l},\ \pi_2=\frac{E}{\gamma l},\ \pi_3=\mu,\ \pi_4=\frac{c}{E},\ \pi_5=\varphi,\ \pi_6=\frac{\sigma}{\gamma l},\ \pi_7=\varepsilon. \tag{4}$$

When similarity is satisfied, these dimensionless parameters remain equal between the model and the prototype. This leads to the following proportional relationships between physical quantities:

$$\frac{S_\delta}{S_l}=1,\ \frac{S_E}{S_\gamma S_l}=1,\ S_\mu=1,\ \frac{S_c}{S_E}=1,\ S_\varphi=1,\ \frac{S_\sigma}{S_\gamma S_l}=1,\ S_\varepsilon=1. \tag{5}$$

After repeated comparison, the geometric similarity ratio $S_l = 1/50$ and the unit weight similarity ratio $S_\gamma = 1$ were selected for this experiment. Then, other similar parameters could be achieved by Eq. (5), as listed in Table 1.

Although the physical model test was generally designed according to similarity theory, some physical parameters inevitably deviated from their theoretical similarity ratios due to the constraints of 1g gravity conditions. As summarized in Table 1, key quantities (geometric dimension, displacement, Young's modulus, stress, and strain) are essential for reproducing the mechanical response of the prototype and were carefully scaled to meet the similarity criteria. However, dimensionless π groups involving gravity, particularly $\pi_2 = E/(\gamma l)$ and $\pi_6 = \sigma/(\gamma l)$, could not be fully satisfied due to limitations in replicating both stiffness and self-weight at model scale. These deviations may affect absolute values of deformation, but the overall deformation patterns and interaction mechanisms remain valid. In contrast, strain ($\pi_7 = \varepsilon$), Poisson's ratio ($\pi_3 = \mu$), and friction angle ($\pi_5 = \varphi$) are dimensionless or material-specific and were accurately preserved in the model. The cohesion–stiffness ratio $\pi_4 = c/E$, while relevant, has limited influence in dry sand due to its low cohesion and is considered a secondary factor. This classification of π groups clarifies which parameters are most important to match and helps explain how the model can still reliably reflect the prototype behavior despite partial deviations. The specific material parameter values of this experiment are shown in Table 2.

The partial mismatch in similarity conditions, particularly those related to stiffness-based π terms, can result in systematic deviations in the experimental results. For example, the underestimated initial tangent modulus of the model soil under 1g gravity may cause smaller ground deformations and weaken the accuracy in representing soil–structure interaction. This can affect the model's ability to reproduce the deformation behavior, failure patterns, and interaction thresholds observed in the full-scale prototype.

Despite this, the impact of such deviations is relatively limited in the case of dry sand. During shield tunneling, sand deformation is mainly controlled by plastic yielding and particle rearrangement, rather than elastic behavior. Therefore, a moderate overestimation of stiffness does not significantly compromise the qualitative accuracy of the test. To further reduce possible errors, quasi-static loading was applied, material properties were carefully adjusted, and a prototype-scale numerical model was developed to cross-check and calibrate the experimental data.

2.3 Scheme of model tests

A total of 17 model tests were conducted, as shown in Table 3 and Fig. 3. These included one greenfield test, eight semicircular arch bridge tests, and eight circular arch bridge tests. Test variables included building eccentricity, foundation type, and building weight.

Step 1: Once the assembly of the model box was complete, a layer of 13 cm-thick experimental sand was placed at the base of the model box. Subsequently, the tunnel model was situated in the designated location and an amount of water equal to the volume of ground loss was introduced into the rubber fluid bladder on the tunnel wall via the reserved pipe.

Step 2: Sand was filled evenly into the box with a constant falling height to ensure uniform compaction across all tests.

Step 3: Once the sand surface was leveled, the arch bridge model, including superstructure and foundation, was positioned. The separate footing bridge rested on the sand surface, while the spread foundation was embedded below. Both components were made of identical materials and scaled according to similarity principles. The underside of the foundation was roughened to increase soil-structure friction, simulating horizontal and vertical freedom for deformation.

Step 4: A tripod and camera were set up to capture stable images. The water-stopping clip was opened to release fluid, simulating tunnel-induced ground loss. Deformations of the soil and bridge were recorded at five-minute intervals using automated imaging. When measurements stabilized over a 30-min period, the test ended. The sand was then removed, and the process was repeated under new conditions.

Table 1
Similarity relation and ratio of physical parameters.

Type	Physical quantity	Symbol	Similarity relation	Similarity ratio
Geometric property	Geometric dimension	l	S_l	1/50
	Displacement	δ	$S_\delta = S_l \cdot S_\varepsilon$	1
Material property	Unit weight	γ	S_γ	1
	Young's modulus	E	$S_E = S_\gamma \cdot S_l$	1/50
	Poisson's ratio	μ	$S_\mu = 1$	1
	Cohesion	c	$S_c = S_E$	1/50
	Friction angle	φ	$S_\varphi = 1$	1
	Stress	σ	$S_\sigma = S_\gamma \cdot S_l$	1/50
	Strain	ε	$S_\varepsilon = 1$	1

Table 2
Material parameter and similarity ratio of the physical model.

	Parameter	Prototype	Models	Similarity ratio	
				Theoretical	Actual
Bridge	γ (kN/m^3)	25.0	19.5	1	0.780
	E (GPa)	53.0 (Tran et al., 2014)	0.935	1/50	0.018
	μ	0.30	0.26	1	0.867
Sand	γ (kN/m^3)	–	18.7	1	1
	φ (°)	–	32.8	1	1
	c (kPa)	–	0	1/50	1
	E (MPa)	–	15.25	1/50	1
	μ	–	0.28	1	1

Table 3
Physical model testing plan.

Total No.	Bridge eccentricity	Foundation type	Weight	Bridge type
1	–	–	–	–
8	0, 0.4	Separate footing Spread foundation	SW, 2SW	Semi-circular arch bridge
8	0, 0.4	Separate footing Spread foundation	SW, 2SW	Circular arch bridge

Note: SW represents self-weight.

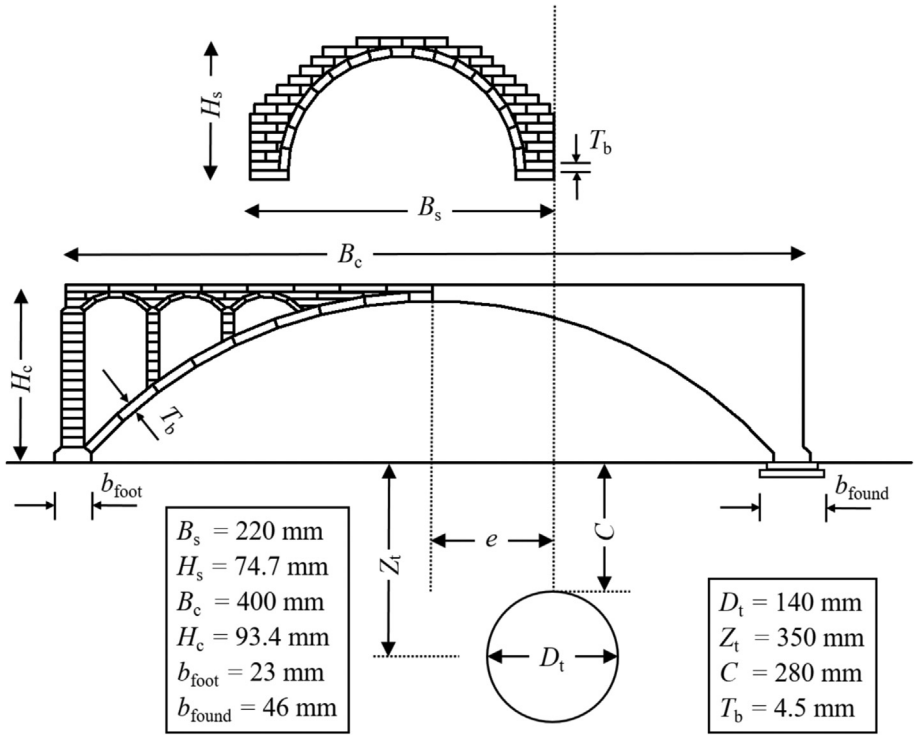

Fig. 3. Test layout in model scale dimensions. (Note: B_s – building width of semi-circular arch bridge; H_s – height of semi-circular arch bridge; B_c – building width of circular arch bridge; H_c – height of circular arch bridge; b_{foot} – width of separate footing; b_{found} – width of spread foundation; D_t – diameter of tunnel; Z_t – depth of the tunnel axis; C – cover depth of tunnel crown; T_b – thickness of building element).

Step 5: The captured images were processed using the PIVlab toolbox in MATLAB. Displacement rates, shear strain, and volumetric strain of the soil and bridge were calculated to evaluate the effects of tunnel excavation on adjacent structures.

3 Model test results for the final state of each group

3.1 Surface soil displacement

This section presents the vertical displacement U_z and horizontal displacement U_x of the foundation (comprising a separate footing and a spread foundation) and the underlying soil in the event of a tunnel volume loss $V_l = 3\%$. Figure 4 illustrates the displacement of a semi-circular masonry arch bridge under varying self-weight and eccentricity conditions.

The surface displacement curves depicted in Fig. 4 diverge from the foundation displacements to a notable extent. This discrepancy can be attributed primarily to the inaccuracies introduced by the image analysis process, particularly in regard to the narrow gap between the model frame building and the model box. Similarly, other physical model tests have also demonstrated this issue (Ritter et al., 2017).

In order to facilitate an accurate description of the soil-bridge interaction, it is first necessary to discuss the issue of foundation settlement. As illustrated in Fig. 4(a)–(d), the mean settlement of the spread foundation is less than that of the separate footing. This is due to the fact that the average soil-foundation contact pressure is lower when a spread foundation is utilized (the contact area of a spread foundation is approximately twice that of a separate footing). On one hand, foundation settlement has a significant increase when the deadweight of the bridge increases, a situation that is more evident during the testing of the spread foundations. The above phenomenon may be attributed to the wider shear stress redistribution in the soil due to the larger contact area, resulting in a more significant settlement response of the foundations when the load is increased.

On the other hand, when $e/B_s = 0$, the foundation settlement on both sides of the bridge is more uniform, and the masonry arch bridge remains horizontal under specific circumstances. However, when $e/B_s = 0.4$, the foundation on the side of the bridge closer to the tunnel centerline exhibits a greater degree of settlement, which also results in a certain degree of inclination of the bridge. This phenomenon can be attributed to the settlement curve of the tunnel, whereby the value of ground settlement is greatest in the vicinity of the tunnel centerline.

A notable difference in vertical displacement is observed between the bridge models with separate footings and those with spread foundations. This discrepancy is concentrated in the region between the footings. For the separate footing model, the maximum surface settlement occurs directly beneath the foundations, and the settlement curve shows

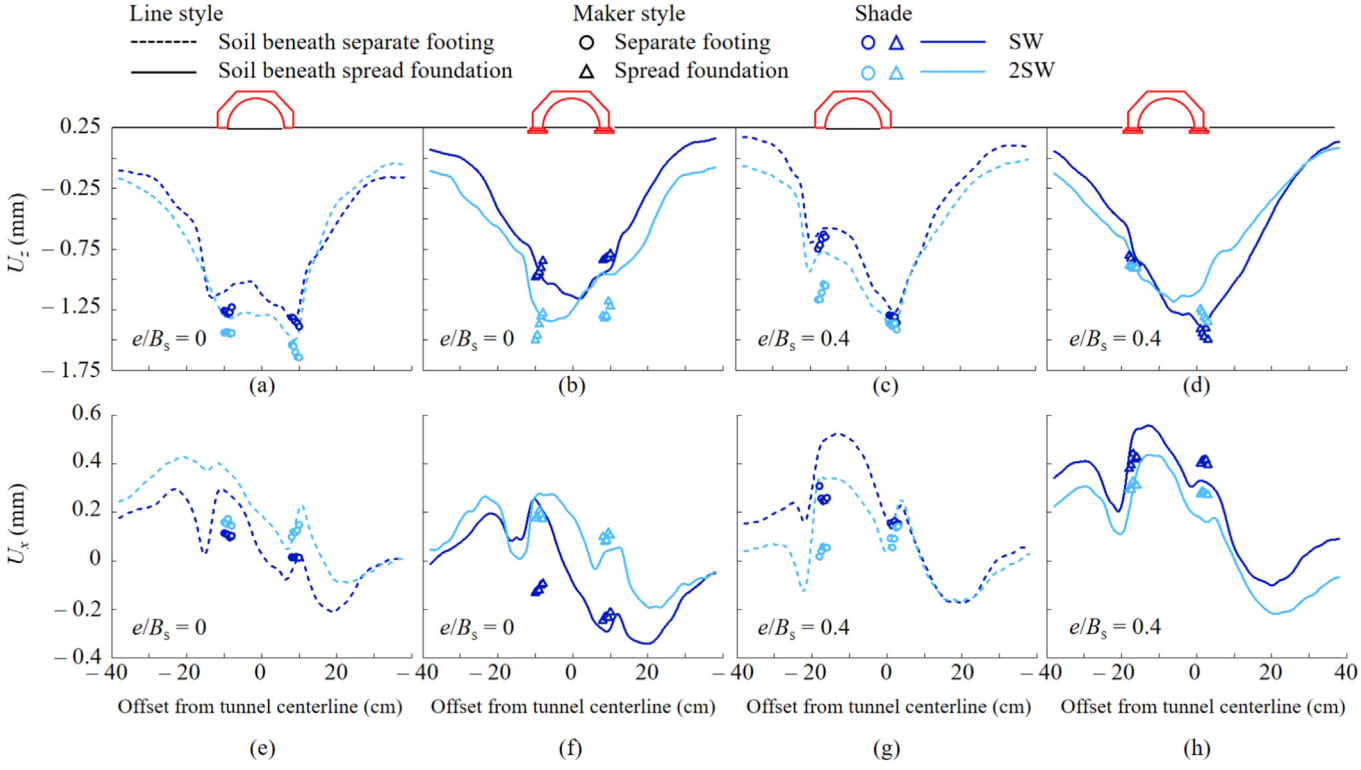

Fig. 4. Foundation and underlying soil displacements with different building weights for the semi-circular arch bridge at $V_l = 3\%$. (a) Separate footing, $e/B_s = 0$, U_z, (b) spread foundation, $e/B_s = 0$, U_z, (c) separate footing, $e/B_s = 0.4$, U_z, (d) spread foundation, $e/B_s = 0.4$, U_z, (e) separate footing, $e/B_s = 0$, U_x, (f) spread foundation, $e/B_s = 0$, U_x, (g) separate footing, $e/B_s = 0.4$, U_x, and (h) spread foundation, $e/B_s = 0.4$, U_x.

a downward trend between them. In contrast, for the spread foundation, the surface settlement increases toward the tunnel axis, with the maximum displacement occurring directly above the tunnel.

As shown in Fig. 4(e)–(h), the horizontal displacement (U_x) profiles are generally similar across different foundation types. Structural rigidity reduces ground surface displacement beneath the foundation, especially in the case of separate footings. However, the low friction of the sand layer causes a clear difference between the displacements of the foundation and the adjacent soil. Therefore, horizontal displacement data from the foundation are primarily used to reflect general trends.

Changes in bridge parameters significantly affect horizontal displacement. For example, increasing the self-weight of the bridge leads to greater displacement differences between foundations. Similarly, variations in eccentricity can intensify horizontal displacement differences. These findings provide valuable insight for evaluating and optimizing the design of arch bridge foundations under tunneling influence.

Figure 5 presents the soil-foundation interaction for the circular arch bridge model. Due to structural differences, the displacement responses of circular and semicircular arch bridges differ. The circular arch bridge exhibits a wider settlement trough, with a sharp increase in vertical displacement at the foundation location. For both foundation types, the maximum surface settlement is located above the tunnel axis.

Under the condition of $e/B_c = 0.4$, the foundation closest to the tunnel axis experiences a settlement nearly equal to the peak surface settlement, while the foundation farther from the tunnel shows minimal displacement. Despite structural differences, the inclination values (q), calculated using Eq. (6), are nearly equal for the two bridge types because the width of the circular arch (B_c) is approximately twice that of the semicircular arch (B_s). When the tunnel is directly beneath the bridge, the inclinations are 0.312‰ for the semicircular arch and 0.210‰ for the circular arch. At $e/B = 0.4$, the inclinations rise to 2.863% and 2.089%, respectively.

$$q = \frac{\Delta U_z}{B} = \frac{|U_{z0} - U_{z1}|}{B}, \tag{6}$$

where U_{z0} and U_{z1} are the average settlement values of the foundations on the left and right sides of the bridge, respectively, and B is the length of the bridge.

Overall, Figs. 4 and 5 reveal the following trends in soil-bridge interaction due to tunneling: (1) Spread foundations help reduce building settlement. (2) Increased bridge self-weight amplifies both vertical and horizontal displacements. (3) The eccentricity of the bridge significantly affects differential settlement and lateral displacement behavior.

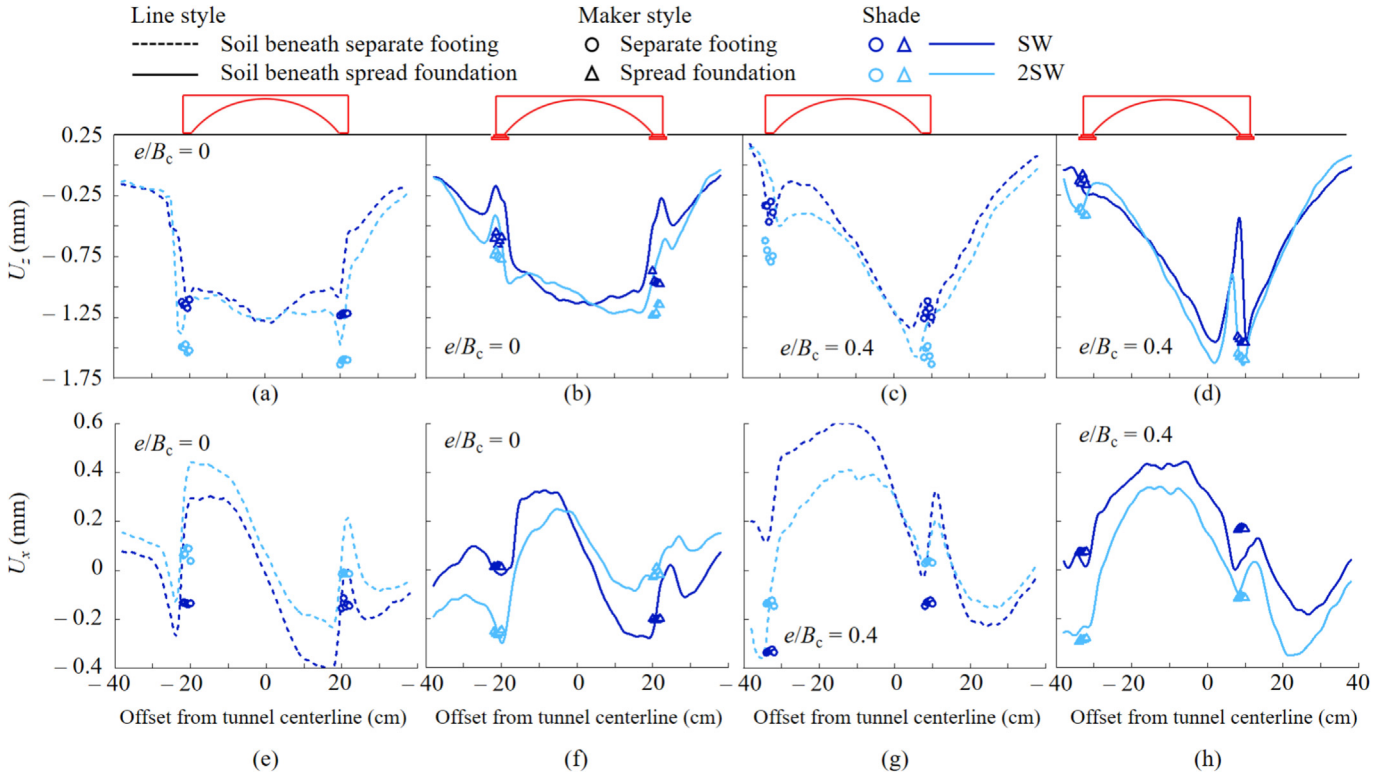

Fig. 5. Foundation and underlying soil displacements with different building weights for the circular arch bridge at $V_l = 3\%$. (a) Separate footing, $e/B_c = 0$, U_z, (b) spread foundation, $e/B_c = 0$, U_z, (c) separate footing, $e/B_c = 0.4$, U_z, (d) spread foundation, $e/B_c = 0.4$, U_z, (e) separate footing, $e/B_c = 0$, U_x, (f) spread foundation, $e/B_c = 0$, U_x, (g) separate footing, $e/B_c = 0.4$, U_x, and (h) spread foundation, $e/B_c = 0.4$, U_x.

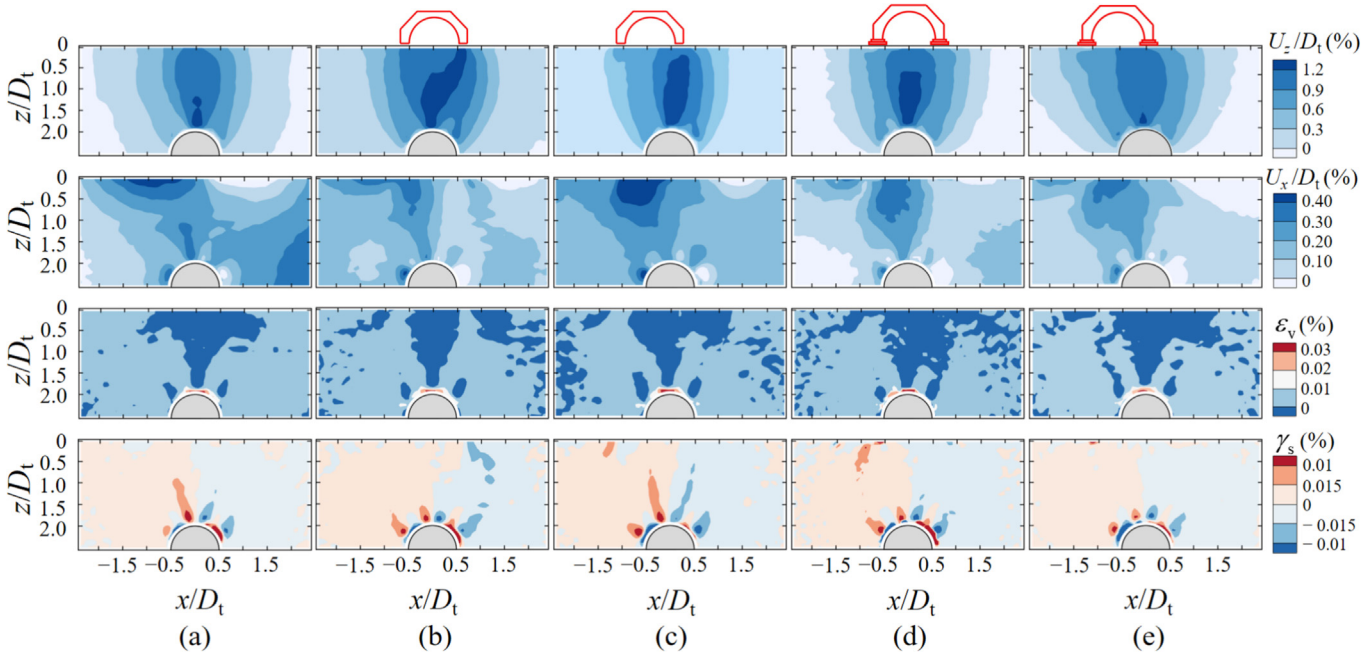

Fig. 6. Soil displacement normalized by tunnel diameter, sample shear, and sample strains for the semi-circular arch bridge at $V_l = 3\%$. (a) Greenfield, (b) separate footing, $e/B_s = 0$, SW, (c) separate footing, $e/B_s = 0.4$, SW, (d) spread foundation, $e/B_s = 0$, SW, and (e) spread foundation, $e/B_s = 0.4$, SW.

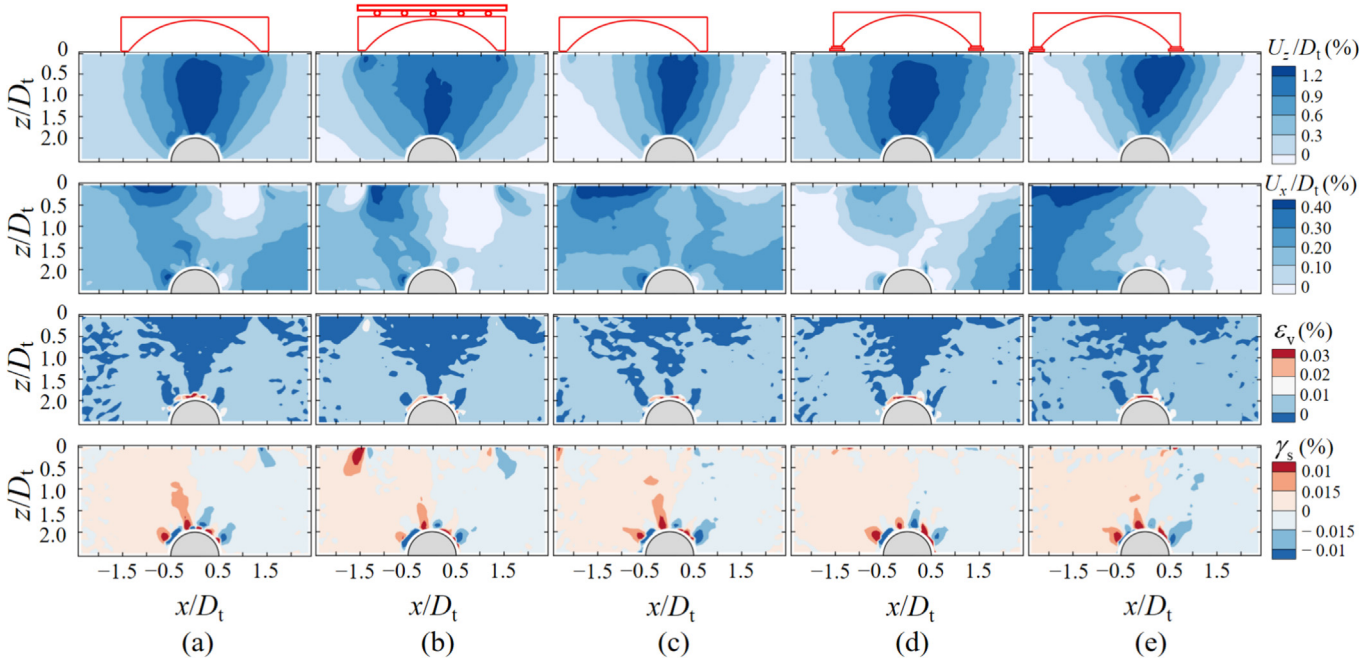

Fig. 7. Soil displacement normalized by tunnel diameter, sample shear, and sample strains for the circular arch bridge at $V_l = 3\%$. (a) Separate footing, $e/B_c = 0$, SW, (b) separate footing, $e/B_c = 0$, 2SW, (c) separate footing, $e/B_c = 0.4$, (d) spread foundation, $e/B_c = 0$, and (e) spread foundation, $e/B_c = 0.4$.

3.2 Subsurface soil displacement contours

Figures 6 and 7 show the distribution of displacements (vertical U_z and horizontal U_x) and strain (shear γ_s and volume ε_v) of the test soil for a tunnel volume loss of $V_l = 3\%$.

In Figs. 6 and 7, the positive vertical and horizontal displacements are downward and to the right, respectively. The negative volumetric strain indicates contraction, and the positive shear strain is to the right.

Figure 6(a) shows that greenfield settlement follows an inverted bell-shaped pattern, with maximum settlement occurring above the tunnel centerline and decreasing outward. Soil on both sides moves laterally toward the tunnel cavity, with more pronounced displacement near the tunnel

walls. The strain distribution highlights the disturbance zone caused by excavation. Tensile strains dominate near the tunnel crown due to prior consolidation, leading to increased voids between soil particles. In contrast, soil above this zone is compressed, resulting in denser packing. Shear stress is symmetrically distributed, with peak values concentrated near the tunnel shoulders (Xu et al., 2021a).

In the presence of a semicircular arch bridge, as shown in Fig. 6(b), soil deformation is amplified compared to the greenfield condition. The self-weight of the bridge increases settlement beneath the foundations. The bridge structure also constrains surface-level horizontal displacements, although deeper soil layers are less affected. Foundation axial forces modify the volumetric strain distribution, concentrating soil compaction between the two footings.

Figure 6(c) illustrates the influence of structural eccentricity on soil response. When $e/B_s = 0.4$, horizontal displacement increases significantly compared to the symmetric case. Settlement above the tunnel axis is also enhanced, forming a distinct shear zone at the tunnel crown.

Finally, the effect of foundation type is considered. The spread foundation reduces settlement beneath the arch by distributing loads more uniformly across the underlying soil. It also limits horizontal displacement and induces shear stress beneath the foundation, similarly to the separate footing, but with a more uniform distribution.

Finally, the effect of foundation type is considered. The spread foundation reduces settlement beneath the arch by distributing loads more uniformly across the underlying soil. It also limits horizontal displacement and induces shear stress beneath the foundation, similarly to the separate footing, but with a more uniform distribution.

Figure 7 illustrates soil-structure interaction under a large-span circular arch bridge. Due to the increased bridge weight and wider footing spacing, the soil settlement zone expands, shear stress becomes more evenly distributed, and stress concentration effects are reduced. However, localized increases in shear stress still occur near the bridge foundations and the tunnel lining. Overall, compressive strain increases but is more uniformly spread, rather than concentrated above the tunnel.

The influence of bridge self-weight on separate footings is also examined. Comparing Fig. 7(a) and (b), higher structural weight leads to increased settlement, shear, and volumetric strain directly beneath the foundations. Interestingly, while settlement near the foundation rises, settlement above the tunnel axis decreases. Two mechanisms explain this behavior: (1) Greater self-weight causes precompression of the soil above the tunnel before excavation, which reduces its post-excavation settlement potential. (2) Increased loading promotes a stronger soil arch effect above the tunnel, distributing loads more widely and reducing vertical displacement at the tunnel axis (Dai et al., 2024).

In order to more accurately assess the degree of soil deformation under various bridge configurations, Fig. 8 depicts the actual strata volume loss as a change of depth.

Figure 8(a) shows that in the greenfield condition, the actual strata volume loss closely matches the designed tunnel volume loss ($V_l = 3\%$). When an arch bridge is present, the true strata volume loss increases, especially with greater bridge self-weight. However, replacing a separate footing with a spread foundation effectively reduces this increase.

Comparing Fig. 8(a) and (b), circular arch bridges cause more surface strata loss than semicircular arches. Additionally, as shown in Fig. 8(a) and (c), construction eccentricity has minimal influence on the actual volume loss.

Lastly, all curves in Fig. 8 exhibit decreasing slopes with increasing depth. Most of the soil volume reduction occurs in the range $0.6 \leq Z/Z_t \leq 0.8$, indicating that compression is concentrated near the tunnel crown. This pattern is consistent with the surface subsidence characteristics observed in Figs. 6 and 7.

3.3 Masonry arch bridge response to tunneling

Figure 9(a) and (b) presents the vertical displacement curves of the main arches for semicircular and circular arch bridges, respectively, under a tunnel volume loss of $V_l = 3\%$. In both cases, the maximum vertical displacement occurs at the centerline of the arch bridge and gradually decreases away from this point. This indicates that the effect of tunnel excavation on arch deformation is concentrated near the tunnel axis.

As shown in Fig. 9(a), increasing the self-weight of the bridge leads to greater vertical displacement of the arch ring. It also increases the difference in displacement between the arch crown and foot, which may compromise the structural stability of the bridge. Additionally, both bridge types exhibit similar trends in displacement reduction when tunnel eccentricity increases. At $e/B = 0.4$, the maximum vertical displacement of the main arch ring decreases significantly compared to the symmetric case.

A comparison between Fig. 9(a) and (b) reveals that, under the same self-weight and eccentricity conditions, the circular arch bridge experiences larger vertical displacement than the semicircular arch bridge. Moreover, the differential settlement between the arch crown and foot is more significant in the circular arch. These observations suggest that circular arches possess lower structural stiffness under tunneling-induced disturbance, leading to a more pronounced deformation response.

Figure 10 presents the strain distributions of semicircular and circular arch bridges with double self-weight under symmetric tunnel conditions ($e/B = 0$). In the semicircular arch bridge, the regions most susceptible to strain are the arch crown and foot. Tensile strain is concentrated at the crown due to vertical settlement and horizontal ground movement, while the arch foot experiences compressive strain caused by lateral thrust. Additionally, tensile stress

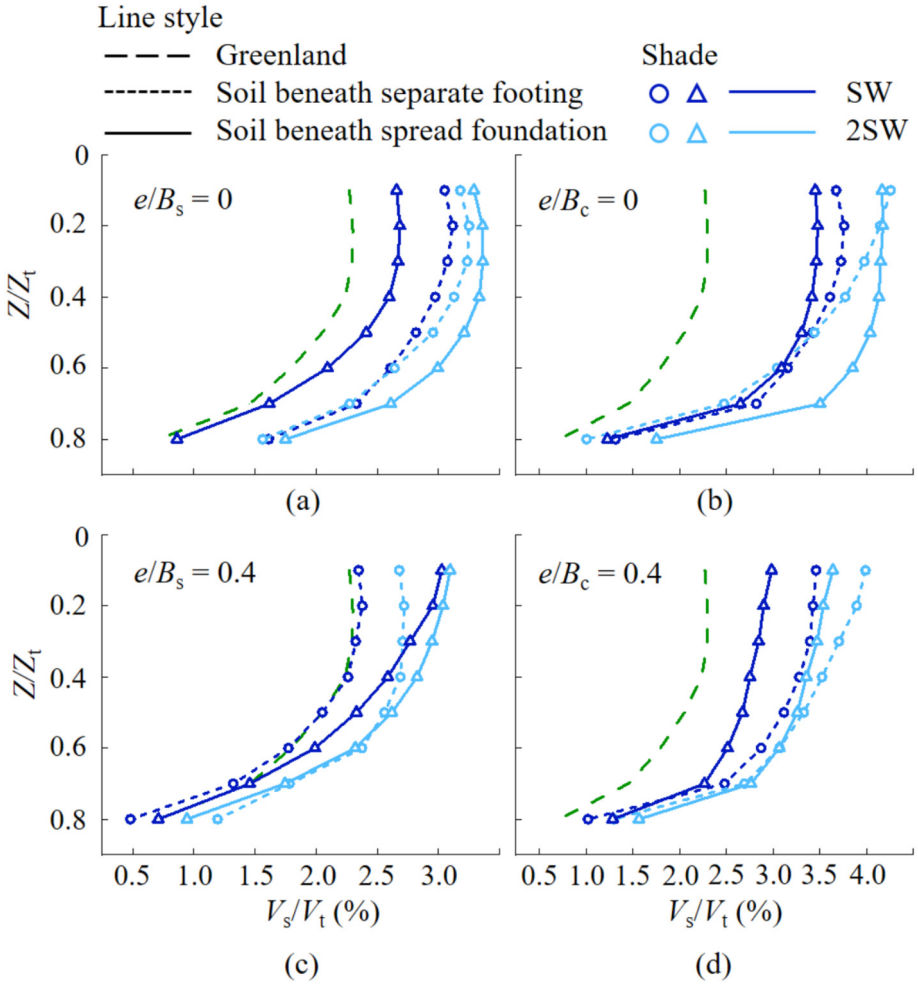

Fig. 8. Soil volume loss with varying depths at $V_l = 3\%$. (a) Semi-circular arch bridge, $e/B_s = 0$, SW, (b) circular arch bridge, $e/B_c = 0$, 2SW, (c) semi-circular arch bridge, $e/B_s = 0.4$, and (d) circular arch bridge, $e/B_c = 0.4$.

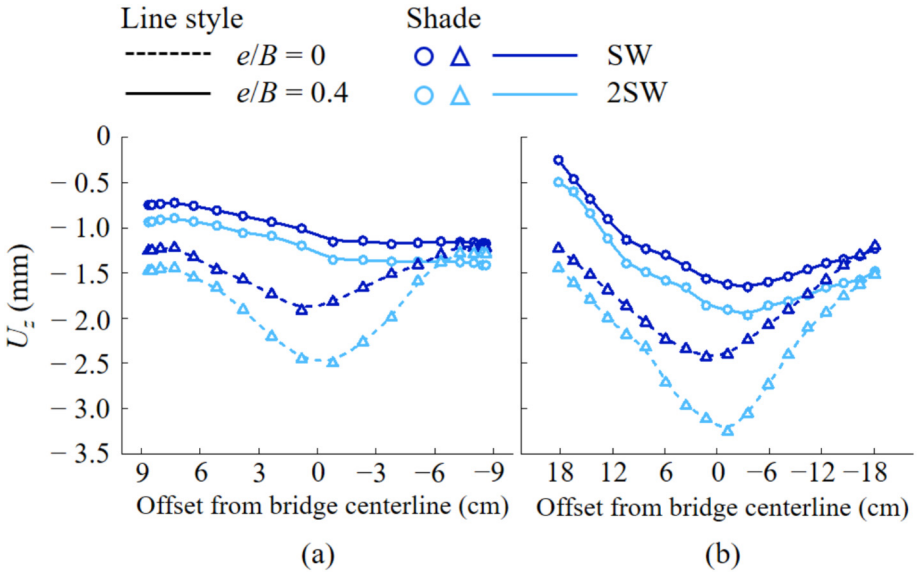

Fig. 9. Vertical settlement of the main arch ring at $V_l = 3\%$. (a) Semi-circular arch bridge, separate footing, and (b) circular arch bridge, separate footing.

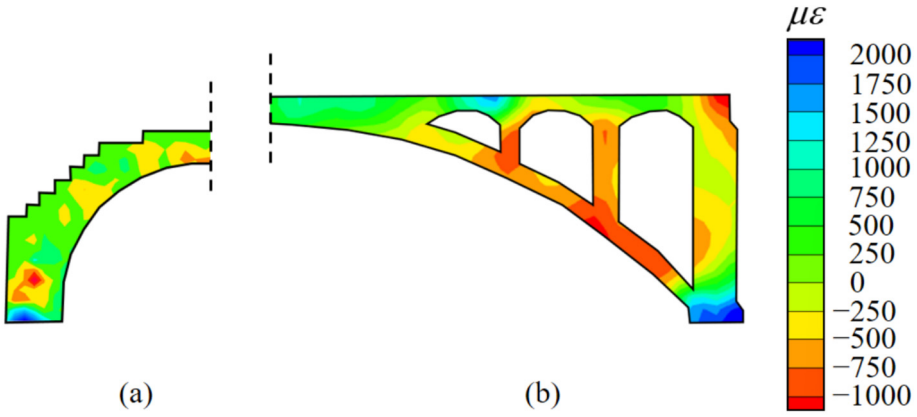

Fig. 10. Simple strain distribution for masonry arch bridge at $V_l = 3\%$. (a) Semi-circular arch bridge, separate footing, $e/B_s = 0$, and (b) circular arch bridge, separate footing, $e/B_c = 0$.

concentrations are observed near the arch shoulders. As horizontal displacement at the arch foot increases, the risk of cracking in these regions grows, potentially leading to structural failure.

The circular arch bridge exhibits a more complex strain pattern due to its structural configuration. In addition to arch foot displacement, the arch ring also supports vertical loads transferred from the deck through columns. This results in two distinct strain characteristics. First, the main arch segment connected to the columns tends toward tension, with peak tensile strain occurring at approximately one-quarter of the arch span. Second, the bridge deck displays compressive behavior, with compressive strain intensifying near the bridge axis. The resulting stress differential between the deck and columns may induce relative displacement and crack formation at their interfaces, compromising structural integrity.

To better quantify the deformation of masonry arch bridges under various conditions, a damage classification system was applied based on tensile strain observed on the bridge façade. The classification thresholds were adopted from Boscardin and Cording (1989), as summarized in Table 4.

Using these thresholds, tensile strain zones were identified across 16 test scenarios, and the proportion of façade areas falling into each damage category is shown in Fig. 10. The results indicate that while tunnel excavation induces localized tensile strains, most of these strains fall within the "Negligible" category. For semicircular arch bridges, under symmetric tunnel conditions ($e/B = 0$), the area classified as "Slight" damage accounts for only about 7% or less of the tensile zone.

Table 4
Critical tensile strain and categories of damage (Boscardin & Cording, 1989).

Category of damage	Level of damage	Limiting tensile strain, $\mu\varepsilon$
0	Negligible	0–500
1	Very slight	500–750
2	Slight	750–1500
3	Moderate to severe	1500–3000
4	Severe to very severe	>3000

As bridge self-weight increases, the proportion of areas falling into damage categories 1 through 3 also rises, indicating that heavier superstructures are more prone to deformation. In contrast, bridges with spread foundations show lower damage levels than those with separate footings. This is attributed to the ability of spread foundations to reduce overall settlement and control horizontal displacement at the footings, thereby limiting the development of tensile strain in the arch.

A comparison of Fig. 11(a) and (b) shows that, under identical loading and eccentricity, circular arch bridges exhibit a significantly higher percentage of damage category 3–4 areas compared to semicircular arches. This highlights structural vulnerabilities in circular arches, which are associated with their flatter geometry and greater concentration of bending moments and shear forces. These effects intensify tensile stress concentrations, potentially exceeding the material's tensile strength and leading to structural damage.

4 Numerical simulation

4.1 Numerical model and meshing

This section employs numerical simulations to investigate the interaction mechanisms between masonry arch bridges and surrounding soil under various conditions. Given the discontinuous nature of masonry structures—characterized by joints and cracks—the DEM provides an effective means to capture their deformation and damage behavior (Pulatsu et al., 2019; Sarhosis et al., 2019). Following the approach of previous studies (Xu et al., 2021b; Xu et al., 2024), the surrounding soil and tunnel were modeled using the FDM. In this study, a coupled DEM–FDM approach was implemented using 3DEC and FLAC3D (version 9.00.167) developed by Itasca.

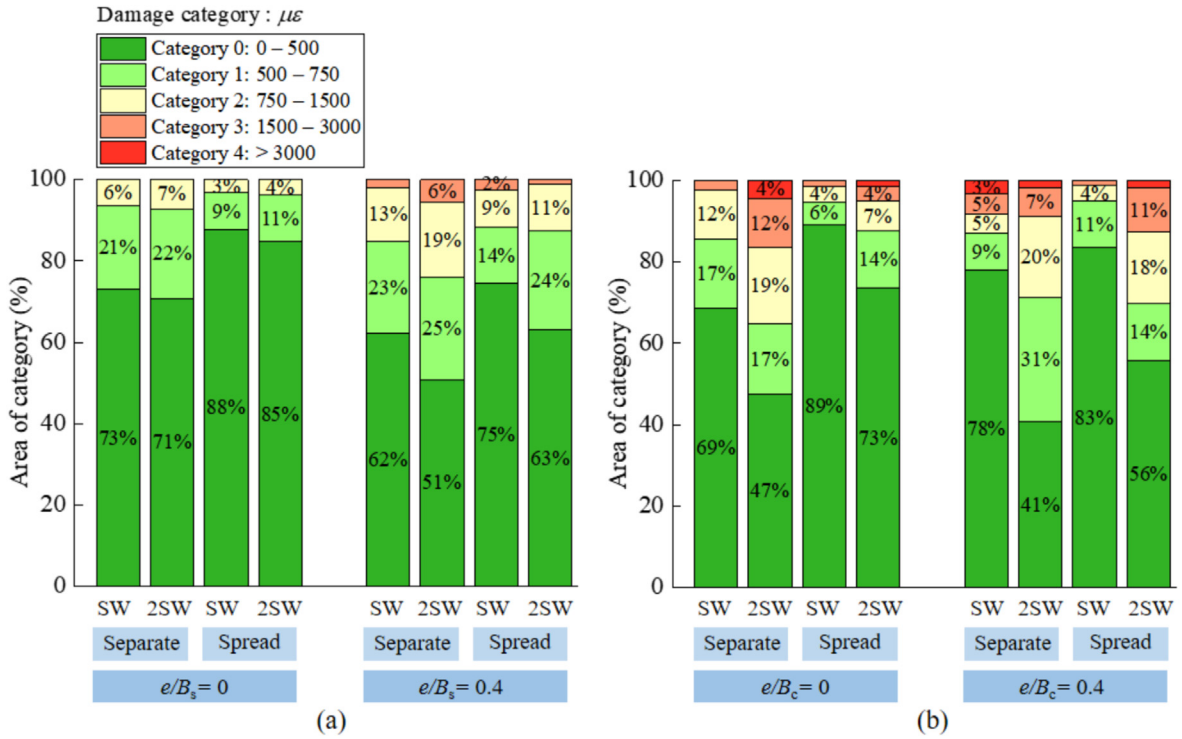

Fig. 11. Building damage bar charts for masonry arch bridge at $V_l = 3\%$. (a) Semi-circular arch bridge, and (b) circular arch bridge.

A numerical model representing a tunnel–greenfield–arch bridge system was constructed, based on the dimensions of the physical tests, using a geometric similarity ratio of CI = 50. The tunnel was modeled as a rigid boundary with a diameter of 7 m, and strata volume loss V_l was simulated using a displacement control method (DCM). The greenfield domain was defined with dimensions of 50 m × 10 m × 30 m. To ensure computational efficiency and accuracy, the model was meshed accordingly. The total number of zones for the greenfield (excluding the tunnel), semicircular arch bridge, and circular arch bridge were 43 630, 2024, and 2028, respectively, as illustrated in Fig. 12.

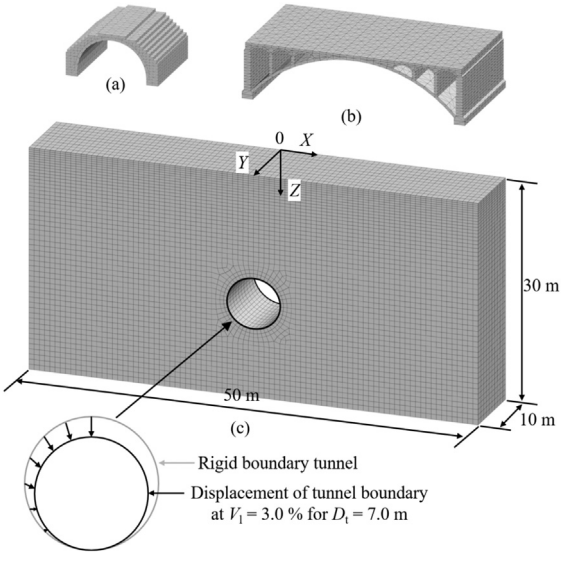

Fig. 12. Meshed models of typical case. (a) Semi-circular arch bridge, (b) circular arch bridge, and (c) soil and tunnel boundary. (Note: The scale of the bridge to soil model was set as 2:1 to better show the bridge mesh details).

4.2 Constitutive material model and model parameters

4.2.1 Material model of masonry arch bridge

Masonry arch bridges are composite structures composed of discrete blocks bonded by mortar. Due to the low tensile strength of the mortar joints, the dominant failure mode is quasi-brittle, often resulting in extensive cracking. Upon failure, the structure behaves as a system of rigid blocks that rotate and slide along crack interfaces. These cracks represent slip surfaces between the blocks.

To simulate this behavior, the current study models the masonry using elastic blocks connected by tension-free frictional interfaces. The block material properties used in the arch bridge prototype are listed in Table 1. The damage evolution is represented through a combination of elastic block deformation and interface failure.

When the structure is subjected to shear or tensile stresses, cohesion is lost at the contacts between blocks. The Coulomb slip criterion is applied to govern the constitutive behavior of these joints. Blocks are assumed to interact at discrete contact points, with soft contact conditions allowing slight overlap. Each contact point is defined by a nor-

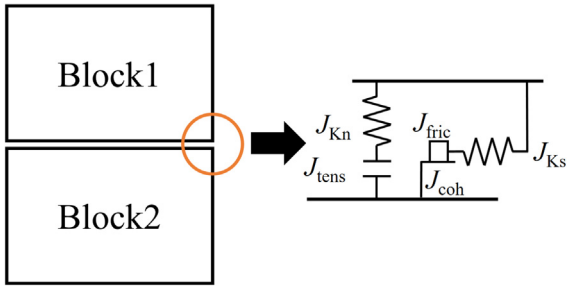

Fig. 13. Joint plane contact model.

mal spring and a shear spring, enabling the transfer of both normal and shear forces between adjacent blocks, as illustrated in Fig. 13.

The joint plane deformation is controlled by parameters such as normal stiffness (J_{Kn}), shear stiffness (J_{Ks}), and cohesion. The joint material parameters shown in Table 5 are derived from physical tests conducted by Tran et al. (2014) on stone masonry arch bridges.

4.2.2 Material model of soil

The HS-Small model, as proposed by Schanz (1999), was employed for the simulation of sandy soil behavior. The HS-Small model incorporates the capabilities of the HS model, including the capacity to account for soil hardening characteristics, differentiate between loading and unloading, and assess stiffness based on stress history and stress paths. Additionally, it can consider the behavior of the shear modulus as it declines with strain within a limited range (Yang & Gu, 2013). In recent years, the HS-Small model has been employed extensively in the investigation of diverse soil-structure interaction issues, and its predictions have been demonstrated to align closely with experimental outcomes (Gong et al., 2020). The values of the 11 parameters included in the HS-Small model utilized in this study are provided in Table 6.

Table 5
Material parameters of joint (Tran et al., 2014).

Parameter	Normal stiffness J_{Kn} (GPa/m)	Sheer stiffness J_{Ks} (MPa/m)	Cohesion c (Pa)	Friction φ (°)
Value	52	41	10	20

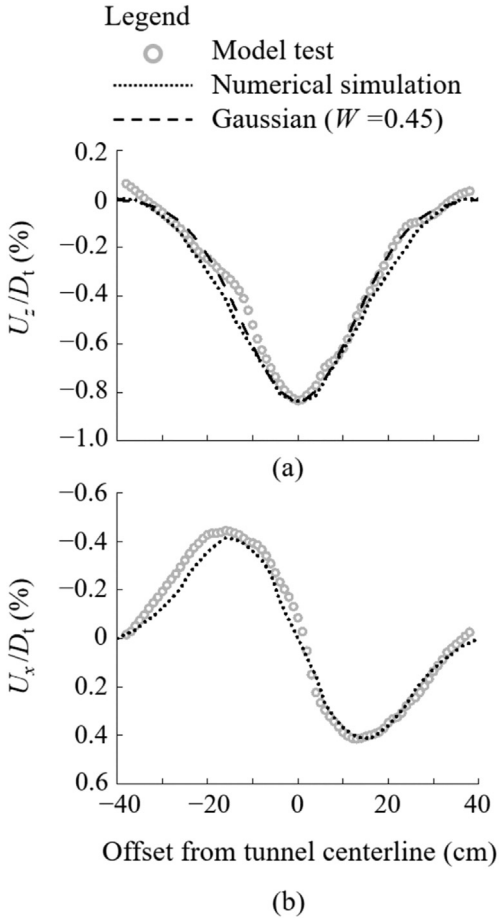

Fig. 14. Comparison between model test measurements and numerical simulation predictions of surface displacement in greenfield test at V_l = 3%. (a) Normalized vertical displacements, and (b) normalized horizontal displacements.

It is important to note that the blocks in the bridge model exhibit a significant disparity in stiffness compared to the surrounding soil. This necessitates the incorporation of a layer of contact surface at the base of the foundation to facilitate the required degree of interaction between the two media. In this study, the foundation-soil interface is modeled using Cullen's friction law, with a friction angle of 15° and values of 65 GPa/m for both tangential and normal stiffness.

Table 6
HS-Small model parameters.

Parameter	γ (kN/m^3)	φ (°)	c (kPa)	E_{oed}^{ref} (MPa)	E_{50}^{ref} (MPa)	E_{ur}^{ref} (MPa)	G_0^{ref} (MPa)	$\gamma_{0.7}$ (10^{-4})	R_f	m	μ	K_0
Sand	18.7	32.8	0	15.25	15.25	61	105	2.00	0.9	0.5	0.28	0.458

Note: E_{oed}^{ref} is reference tangent stiffness for primary oedometer loading, E_{50}^{ref} is the reference secant stiffness in standard drained triaxial test, E_{ur}^{ref} is the reference unloading–reloading stiffness modulus at the reference pressure, G_0^{ref} is the shear stiffness modulus, $\gamma_{0.7}$ is the level of strains where the shear modulus reaches 70% of its initial value, R_f is the damage ratio, m is the Janbu-type parameter, and K_0 is the ratio of initial horizontal to vertical effective stress.

4.3 Validation of the numerical model

In order to validate the current numerical simulation method, the surface displacements due to tunnel excavation obtained from the experimental model and the numerical simulation for the case of a strata volume loss rate $V_l = 3\%$ are compared in Fig. 14(a) and (b).

As evidenced by the results, there is a notable correspondence between the surface deformation curves calculated by the numerical model and the measured results of the physical model tests, particularly in terms of the settlement maximum value and the width of the settlement trough. This highlights the reliability of the numerical model construction and the selection of the intrinsic parameters. Secondly, when the volume loss rate $V_l = 3\%$, the settlement curve calculated by the numerical model is in good agreement with the Gaussian distribution (slot width coefficient $W = 0.45$). In conclusion, the numerical model developed in this study demonstrated satisfactory computational outcomes. Furthermore, the constitutive model and parameters selected by the numerical model are deemed suitable for achieving the objectives of this study.

5 Parametric study and discussion

5.1 Effect of tunnel construction parameters on the safety of masonry bridges

To further evaluate the impact of shield tunneling parameters on the stability of adjacent masonry arch structures, this study examines two key factors: the normalized tunnel burial depth (Z_t/D_t) and the strata volume loss rate (V_l), using the displacement control method.

Previous studies have shown that masonry structures often experience combined shear and compressive loading. Under such stress states, four distinct failure modes may occur: (1) bond tensile failure along joints, (2) shear failure across joint planes, and with increasing normal stress, (3) tensile cracking, and (4) compressive crushing of blocks (Mann & Müller, 1982). These modes suggest that shear and tensile displacements along block interfaces can serve as early indicators of structural vulnerability in masonry arch bridges.

Figure 15 illustrates the relationship between the maximum shear and normal displacements at the joint plane

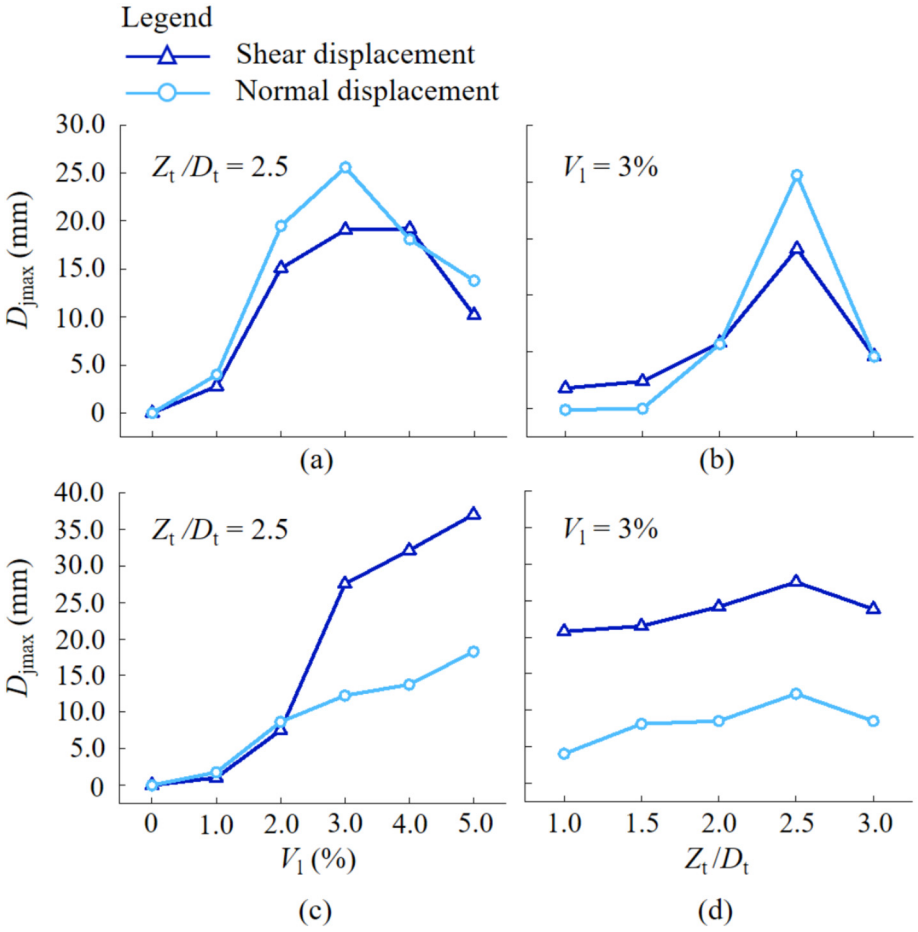

Fig. 15. Maximum displace of joint plane in different tunnel construction parameters. (a)–(b) Semi-circular arch bridge, separate footing, $e/B_s = 0$, and (c)–(d) circular arch bridge, separate footing, $e/B_c = 0$.

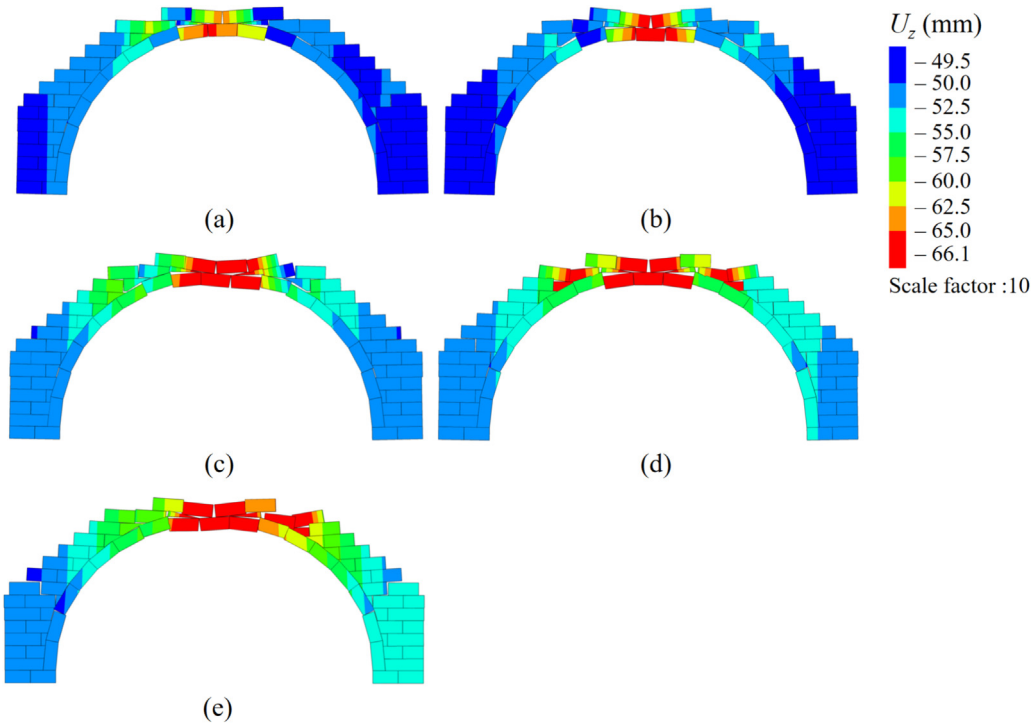

Fig. 16. Vertical displacement distribution of semicircular arch bridges with different strata volume loss rates V_l. (a) $V_l = 1\%$, (b) $V_l = 2\%$, (c) $V_l = 3\%$, (d) $V_l = 4\%$, and (e) $V_l = 5\%$.

D_{jmax} and the parameters V_l and Z_t/D_t. As shown in Fig. 15 (a) and (b), both displacement measures in the semicircular arch bridge initially increase and then decrease with rising V_l and Z_t/D_t. Peak values for both shear and tensile displacements occur at $V_l = 3\%$ and $Z_t/D_t = 2.5$.

This trend can be explained in two phases. When V_l is less than 3% (Fig. 16(a)–(c)), displacement at the arch foundation leads to higher shear and compressive stresses at the joints, especially near the arch crown, resulting in increased joint displacement. Beyond this threshold (Fig. 16(d)–(e)), the stress state becomes more complex, and multiple load paths are activated, leading to tensile cracking at both the arch crown and shoulders. This redistribution of internal forces reduces the maximum joint displacement, aligning with the tensile strain patterns shown in Fig. 10(a).

The influence of normalized tunnel depth Z_t/D_t on joint plane displacement follows a trend similar to that of the stratum volume loss rate V_l. This can be attributed to the constrained deformation zone near shallow tunnels, where increased pressure is applied to the joint interfaces as tunnel depth increases. However, greater tunnel depth also reduces the foundation deformation of the arch bridge. As a result, when $Z_t/D_t > 2.5$, the joint displacement begins to decrease.

Comparing Fig. 15(a) and (c), it is observed that for the circular arch bridge, both maximum shear and normal displacements on the joint plane continue to increase as V_l rises within the range of [0, 5%]. Unlike the semicircular arch bridge, there is no observed reduction in displacement beyond a critical volume loss threshold. This suggests that, under $V_l < 5\%$, the stress distribution in the circular arch bridge has not reached a critical redistribution stage, and the structure continues to respond with increasing deformation.

In order to more clearly elucidate the coupling effect of tunnel construction parameters on arch bridges, Gaussian fitting is performed based on the calculated nodal displacement results D_s under different volume loss rates and normalized tunnel burial depths, and the fitting equations are shown in Eq. (7). This process yields the three-dimensional surface distribution illustrated in Fig. 17, and the corresponding fitted parameters are listed in Table 7.

$$\begin{aligned} D_s = D_0 + A \times \exp(-0.5 \times ((V_l \times \cos(\theta) \\ + Z_t/D_t \times \sin(\theta) - x_c \times \cos(\theta) - y_c \times \sin(\theta))/w_1)^2 \\ -0.5 \times ((-V_l \times \sin(\theta) + Z_t/D_t \times \cos(\theta) \\ + x_c \times \sin(\theta) - y_c \times \cos(\theta))/w_2)^2), \end{aligned} \tag{7}$$

where D_0 is the baseline value, A is the Amplitude, x_c is the center coordinate in Z_t/D_t direction, y_c is the center coordinate in V_l direction, w_1 and w_2 are the standard deviation in rotated x-direction and y-direction, and θ is the rotation angle.

The fitting results confirm that both volume loss rate V_l and normalized tunnel depth Z_t/D_t significantly influence the deformation behavior of semicircular arch bridges.

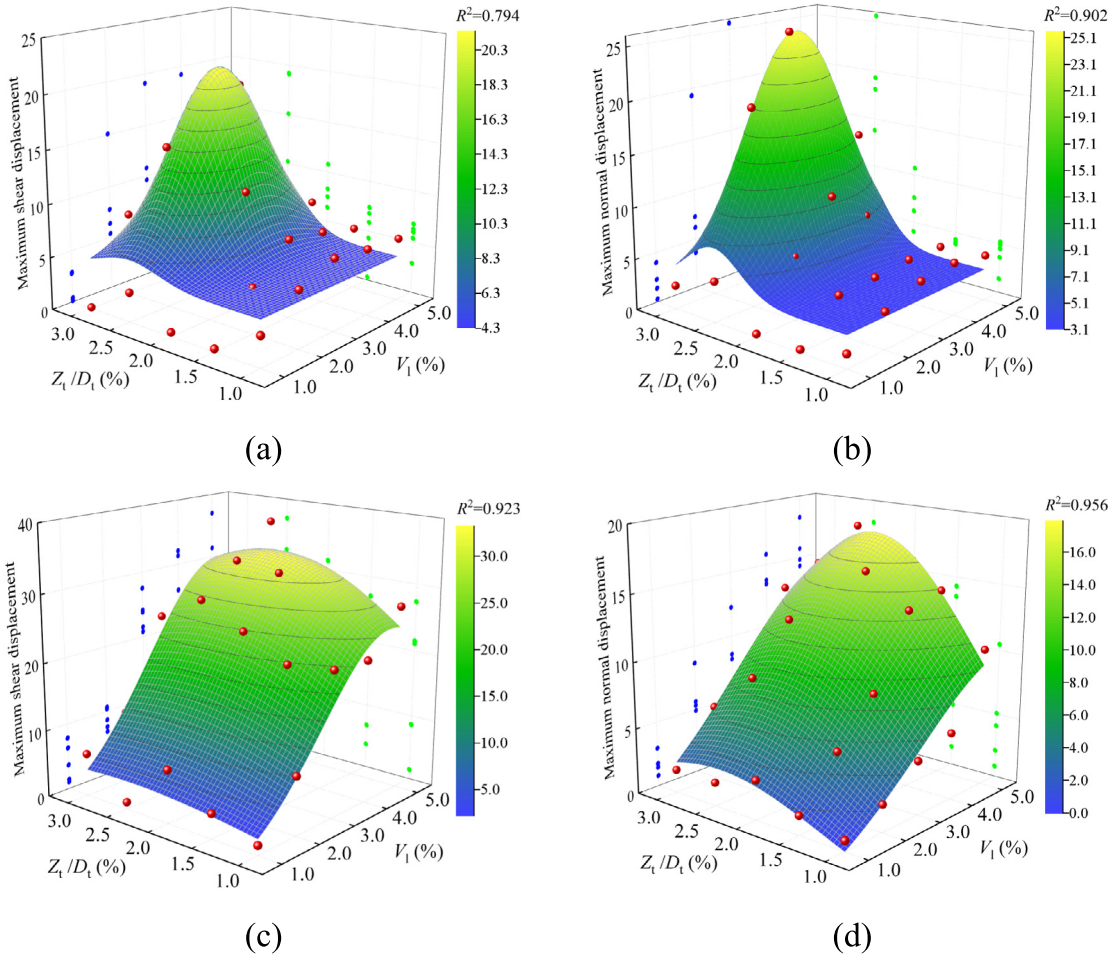

Fig. 17. Maximum displacement of joint plane with the influence of different tunnel construction parameter coupling. (a)–(b) Semi-circular arch bridge, separate footing, $e/B_s = 0$, and (c)–(d) circular arch bridge, separate footing, $e/B_c = 0$.

Table 7
Parameters of Gaussian fitting results of Fig. 17.

Fig. 17	D_0	A	x_c	w_1	y_c	w_2	θ
(a)	4.29	17.04	4.00	0.70	3.41	1.10	0
(b)	3.10	22.44	4.03	0.63	3.21	1.20	0
(c)	−2.57	35.81	3.72	2.00	4.65	3.67	1.54
(d)	−2.97	21.48	3.52	2.93	5.67	2.46	1.86

The extreme value surfaces of shear and normal displacements on the joint interface exhibit a "mountain-shaped" profile, with peak values of 21.33 and 25.54 mm, respectively. In contrast, for circular arch bridges, tunnel depth has a comparatively smaller effect on joint displacement than the volume loss rate.

From the fitted response surfaces, the maximum shear displacement of the joint interface in the circular arch bridge occurs at $V_l = 4.65\%$ and $Z_t/D_t = 2.35$. The peak normal displacement is observed at $V_l = 5.67\%$ and $Z_t/D_t = 2.26$. These findings provide a quantitative basis for assessing structural risk and selecting appropriate design and mitigation strategies during the pre-construction phase of similar tunneling projects.

5.2 Discussion on the characteristics of parameters for different masonry bridges

The intrinsic structural characteristics of masonry arch bridges influence both their load-bearing capacity and damage patterns. To examine these behaviors, the physical and mechanical properties of the masonry blocks and contact interfaces were varied in the simulation.

Figure 18 illustrates the variation in maximum tensile stress and strain of the bridge structures under different scaling factors of Young's modulus. For the semicircular arch bridge, both tensile stress and strain increase with higher values of Young's modulus. This trend is attributed to the reduced deformability of the blocks as stiffness increases, resulting in greater stress concentration, especially in tension zones. The tensile stress continues to rise until the structure fails through shear or tension.

Comparing Fig. 18(a) and (b), the circular arch bridge consistently exhibits higher tensile stress and strain than the semicircular arch bridge under the same Young's modulus scaling factor. This indicates more severe stress concentration in the circular arch. However, beyond a certain magnification factor (k), the growth rate of tensile

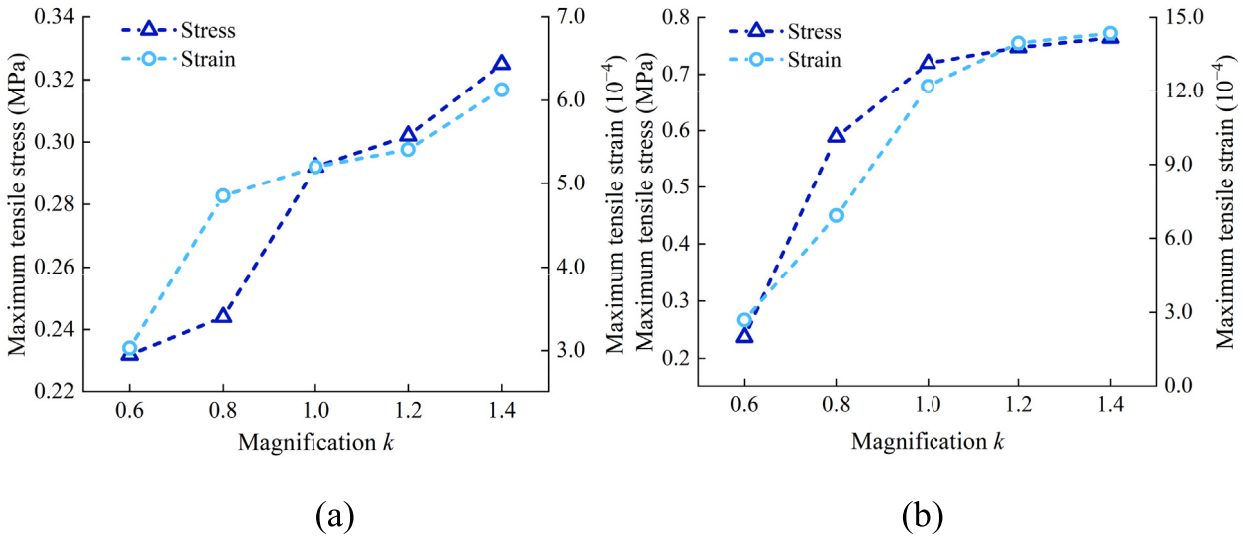

Fig. 18. Maximum tensile stress and strain with different Young's modulus magnification k. (a) Semi-circular arch bridge, separate footing, $e/B_s = 0$, and (b) circular arch bridge, separate footing, $e/B_c = 0$.

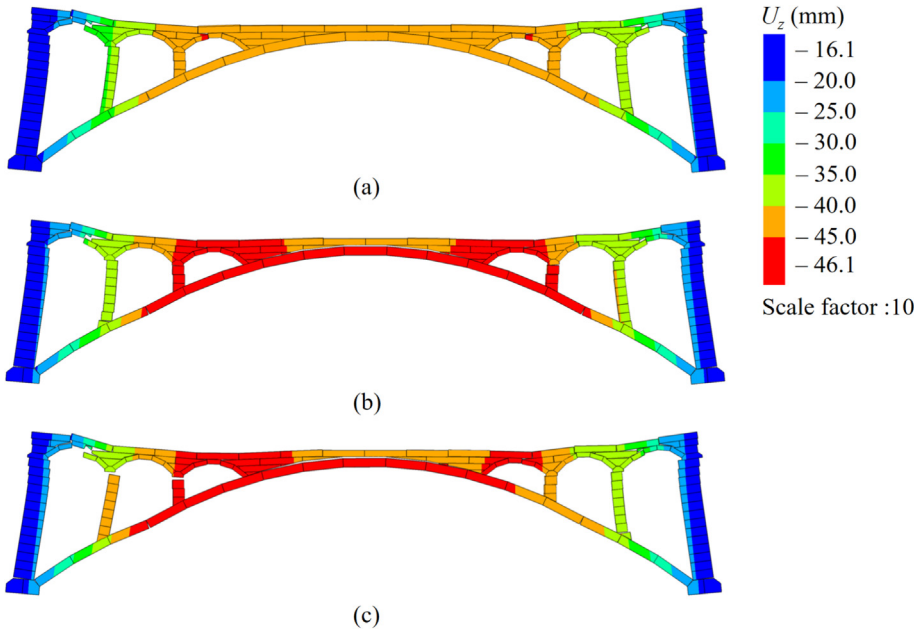

Fig. 19. Vertical displacement distribution of circular arch bridges with different joint stiffness: (a) $J_{Kn} = 72$ GPa/m, $J_{Ks} = 57$ GPa/m; (b) $J_{Kn} = 52$ GPa/m, $J_{Ks} = 41$ GPa/m; (c) $J_{Kn} = 31$ GPa/m, $J_{Ks} = 25$ GPa/m.

stress and strain diminishes and eventually stabilizes. This plateau suggests a practical upper limit for Young's modulus in engineering applications. Exceeding this limit may induce material fracture due to excessive brittleness.

In addition to the influence of block stiffness, the mechanical properties of joints play a key role in governing the deformation and failure behavior of masonry arch bridges. Figure 19 presents simulation results for three circular arch bridge models with varying joint stiffness levels.

The analysis indicates that, due to its relatively low curvature, the circular arch bridge behaves similarly to a simply supported beam. During tunnel excavation, tensile forces develop in the lower part of the bridge, while compressive forces act on the deck slab. This leads to differential displacement between the arch and the deck.

When the stiffness of the joints is high, this displacement difference is partially mitigated, resulting in shear cracks forming on the contact surface between the columns and the bridge deck (Fig. 19(a)). However, as the stiffness of the joints decreases, the shear cracks extend between the columns and the bridge deck, evolving into a series of tension cracks due to the vertical displacement of the main arch (Fig. 19(b) and (c)).

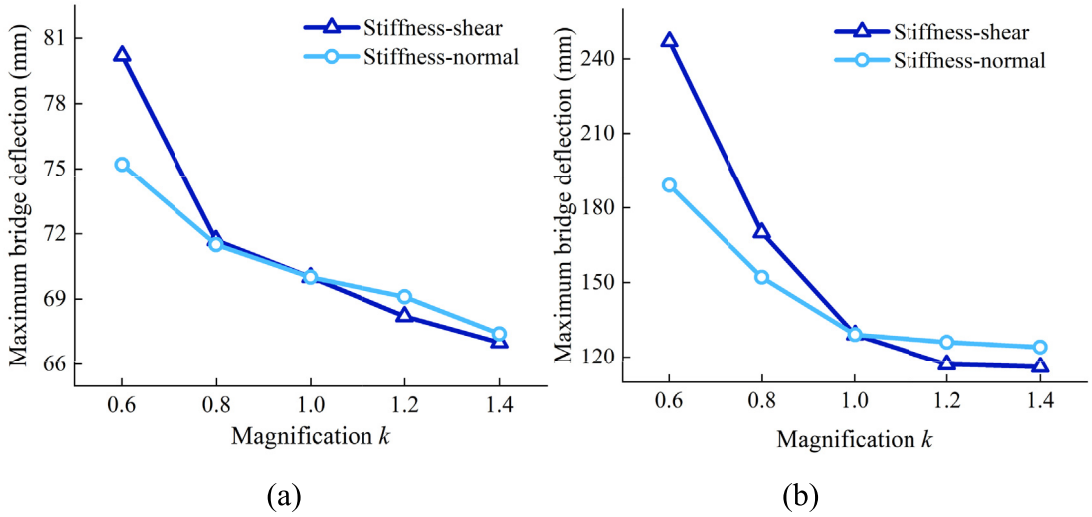

Fig. 20. Maximum deflection of bridge with different joint stiffness magnification k. (a) Semi-circular arch bridge, separate footing, $e/B_s = 0$, and (b) circular arch bridge, separate footing, $e/B_c = 0$.

To better quantify the effect of joint stiffness on structural performance, deflection is adopted as an index to evaluate the safety and serviceability of masonry arch bridges. The computed maximum deflections under varying joint stiffness conditions are presented in Fig. 20.

The results indicate that when the stiffness amplification factor k is less than or equal to 1.0, increasing both shear and normal stiffness reduces the maximum bridge deflection to a certain extent. Notably, shear stiffness has a more pronounced impact on deflection control than normal stiffness. This is because, under tunnel-induced disturbance, the initial deformation of the arch bridge is primarily governed by shear slip along the joints, while normal displacement remains relatively limited. As such, enhancing shear stiffness is more effective in mitigating overall structural deformation. When k exceeds 1.0, the benefit of further increasing joint stiffness diminishes. The deflection trend gradually stabilizes, indicating that the structural system approaches its deformation limit as global stiffness increases.

These findings suggest that joint shear stiffness is a critical parameter in controlling bridge deformation. During the design and maintenance of masonry arch bridges, prioritizing the enhancement of shear stiffness—particularly through high-stiffness materials or grouting techniques—can significantly improve deformation resistance. In areas prone to normal joint cracking, such as the arch crown, increasing normal stiffness should also be considered to enhance structural integrity.

6 Conclusions

In this study, we focus on the complex interaction mechanism between tunnels and masonry arch bridges by constructing a physical model. By observing the displacement and stress redistribution of the real soil body and arch bridge, the deformation mechanism and risk zoning of the structure are revealed. Additionally, a sensitivity analysis of tunnel and bridge parameters was conducted using a coupled finite element-discrete element model. The following conclusions can be drawn.

(1) The arch span is identified as a key factor influencing soil response. Larger spans lead to wider settlement zones and more uniform shear stress distributions, which help mitigate stress concentrations. However, a larger span typically results in a greater self-weight, so in actual projects, the impact of tunnel construction on large-span arch bridges should be conservatively considered.

(2) Masonry semi-circular arch bridge exhibits the highest susceptibility to damage under the influence of tunnel construction at the vault and footing. Tensile strains dominate at the arch crown, especially under heavy loads, while the arch foot is primarily governed by compressive effects due to lateral thrust. Moreover, the simplified beam analogy for circular arches with high span-to-rise ratios provides a new perspective for analyzing displacement incompatibilities and potential cracking at deck-pier joints.

(3) This study reveals a new spatial pattern in the mechanical behavior of masonry arch bridges influenced by tunnel excavation. The displacements at the joint interfaces, which include both shear and tensile cracking, exhibit a three-dimensional Gaussian distribution shaped by the combined effects of tunnel volume loss and burial depth. For circular arch bridges in particular, the displacement of the joint surfaces is found to be more sensitive to volume loss than to burial depth. This differential sensitivity pro-

vides a valuable framework for optimizing tunnel construction parameters in the vicinity of heritage structures.

(4) From a structural material perspective, the research establishes a clear relationship between mechanical enhancement measures and bridge performance. Increasing the Young's modulus of the model material or improving the shear stiffness of masonry joints significantly reduces both deformation and the likelihood of cracking. This strategy is applicable not only in the construction of new infrastructure but also in the preservation and rehabilitation of existing historical structures.

This paper focuses on scenarios involving the construction of circular tunnels in dry sand beneath masonry arch bridges, and bridges are constructed with uniform block sizes. Future work will consider additional factors, such as the size of the building materials, the water content of the strata, the angle of the tunnel, and the comprehensive evaluation index system of risk zoning.

Data availability

The data that support the findings of this study are available from the corresponding author upon reasonable request.

CRediT authorship contribution statement

Si-yi Huang: Writing – review & editing, Writing – original draft, Software, Methodology, Data curation. **Li-yuan Tong:** Writing – review & editing, Project administration, Funding acquisition. **Ming-fei Zhang:** Project administration, Funding acquisition. **Tao Qiu:** Writing – review & editing, Methodology. **Xiao-dong Li:** Project administration. **Jia-jia Wan:** Project administration, Funding acquisition.

Declaration of competing interest

The authors declare that they have no known competing financial interests or personal relationships that could have appeared to influence the work reported in this paper.

Acknowledgement

The authors would like to acknowledge the financial support from the National Natural Science Foundation of China (Grant Nos. 52178384 and 52478388).

References

Amorosi, A., Boldini, D., De Felice, G., Malena, M., & Sebastianelli, M. (2014). Tunnelling-induced deformation and damage on historical masonry structures. *Géotechnique, 64*(2), 118–130.

Augusthus-Nelson, L., & Swift, G. (2020). Experimental investigation of the residual behaviour of damaged masonry arch structures. *Structures, 27*, 2500–2512.

Augusthus-Nelson, L., Swift, G., Melbourne, C., Smith, C., & Gilbert, M. (2018). Large-scale physical modelling of soil-filled masonry arch bridges. *International Journal of Physical Modelling in Geotechnics, 18*(2), 81–94.

Bilotta, E., Paolillo, A., Russo, G., & Aversa, S. (2017). Displacements induced by tunnelling under a historical building. *Tunnelling and Underground Space Technology, 61*, 221–232.

Borlenghi, P., Saisi, A., & Gentile, C. (2023). ND testing and establishing models of a multi-span masonry arch bridge. *Journal of Civil Structural Health Monitoring, 13*(8), 1595–1611.

Boscardin, M. D., & Cording, E. J. (1989). Building response to excavation-induced settlement. *Journal of Geotechnical Engineering, 115*(1), 1–21.

Broere, W. (2016). Urban underground space: Solving the problems of today's cities. *Tunnelling and Underground Space Technology, 55*, 245–248.

Chen, H. M., Yu, H. S., & Smith, M. J. (2016). Physical model tests and numerical simulation for assessing the stability of brick-lined tunnels. *Tunnelling and Underground Space Technology, 53*, 109–119.

Chiu, Y. C., Wang, T. T., & Huang, T. H. (2014). Investigating continual damage of a nineteenth century masonry tunnel. *Proceedings of the Institution of Civil Engineers-Forensic Engineering, 167*(3), 109–118.

Conde, B., Ramos, L. F., Oliveira, D. V., Riveiro, B., & Solla, M. (2017). Structural assessment of masonry arch bridges by combination of non-destructive testing techniques and three-dimensional numerical modelling: Application to Vilanova bridge. *Engineering Structures, 148*, 621–638.

Cui, J., & Nelson, J. D. (2019). Underground transport: An overview. *Tunnelling and Underground Space Technology, 87*, 122–126.

Dai, H., Sun, Y., Rong, Y., Yu, J., Wu, J., & Zhang, Y. (2024). Study on soil pressure of loose soil in cohesive soil tunnel considering soil arch effect. *Frontiers in Earth Science, 12*, 1361227.

Forgács, T., Sarhosis, V., & Bagi, K. (2018). Influence of construction method on the load bearing capacity of skew masonry arches. *Engineering Structures, 168*, 612–627.

Gibbings, J. C. (2011). *Dimensional analysis*. Springer Science & Business Media.

Gong, C., Ding, W., & Xie, D. (2020). Twin EPB tunneling-induced deformation and assessment of a historical masonry building on Shanghai soft clay. *Tunnelling and Underground Space Technology, 98*, 103300.

Liang, R., Xia, T., Hong, Y., & Yu, F. (2016). Effects of above-crossing tunnelling on the existing shield tunnels. *Tunnelling and Underground Space Technology, 58*, 159–176.

Lin, D., Zhou, Z., Weng, M., Broere, W., & Cui, J. (2024). Metro systems: Construction, operation and impacts. *Tunnelling and Underground Space Technology, 143*, 105373.

Liu, B., Sarhosis, V., Booth, A. D., & Gilbert, M. (2024). The 3D response of a large-scale masonry arch bridge–Part II: Performance at failure. *Engineering Structures, 313*, 118308.

Mann, W., & Müller, H. (1982). Failure of shear-stressed masonry: An enlarged theory, tests and application to shear walls. *Proceedings of the British Ceramic Society, 30*, 223–235.

Milani, G., & Lourenço, P. B. (2012). 3D non-linear behavior of masonry arch bridges. *Computers & Structures, 110*, 133–150.

Ng, C. W. W., Lu, H., & Peng, S. Y. (2013). Three-dimensional centrifuge modelling of the effects of twin tunnelling on an existing pile. *Tunnelling and Underground Space Technology, 35*, 189–199.

Pulatsu, B., Erdogmus, E., & Lourenço, P. B. (2019). Simulation of masonry arch bridges using 3D discrete element modeling. In *Structural Analysis of Historical Constructions: An Interdisciplinary Approach* (pp. 871–880). Cham: Springer International Publishing.

Ritter, S., Giardina, G., DeJong, M. J., & Mair, R. J. (2017). Influence of building characteristics on tunnelling-induced ground movements. *Géotechnique, 67*(10), 926–937.

Sarhosis, V., De Santis, S., & de Felice, G. (2016). A review of experimental investigations and assessment methods for masonry arch bridges. *Structure and Infrastructure Engineering, 12*(11), 1439–1464.

Sarhosis, V., Forgács, T., & Lemos, J. V. (2019). Modelling backfill in masonry arch bridges: a DEM approach. In *International Conference on Arch Bridges* (pp. 178–184). Cham: Springer International Publishing.

Sarhosis, V., Liu, B., & Gilbert, M. (2024). The 3d response of a large-scale masonry arch bridge-part I: Performance under low and medium loading levels. *Engineering Structures, 316*, 118496.

Schanz, T. (1999). Formulation and verification of the Hardening-Soil Model. In *RBJ Brinkgreve, Beyond 2000 in Computational Geotechnics* (pp. 281–290).

Sirivachiraporn, A., & Phienwej, N. (2012). Ground movements in EPB shield tunneling of Bangkok subway project and impacts on adjacent buildings. *Tunnelling and Underground Space Technology, 30*, 10–24.

Stamhuis, E., & Thielicke, W. (2014). PIVlab–towards user-friendly, affordable and accurate digital particle image velocimetry in MATLAB. *Journal of Open Research Software, 2*(1), 30.

Sun, Z., Zhang, D., Li, A., Lu, S., Tai, Q., & Chu, Z. (2022). Model test and numerical analysis for the face failure mechanism of large cross-section tunnels under different ground conditions. *Tunnelling and Underground Space Technology, 130*, 104735.

Tran, V. H., Vincens, E., Morel, J. C., Dedecker, F., & Le, H. H. (2014). 2D-DEM modelling of the formwork removal of a rubble stone masonry bridge. *Engineering Structures, 75*, 448–456.

Wang, H., Leung, C. F., Yu, J., & Huang, M. (2020). Axial response of short pile due to tunnelling-induced soil movement in soft clay. *International Journal of Physical Modelling in Geotechnics, 20*(2), 71–82.

Wang, M., Dong, Y., Yu, L., Fang, L., Wang, X., & Liu, D. (2019). Experimental and numerical researches of precast segment under radial dislocation conditions. *Tunnelling and Underground Space Technology, 92*, 103055.

Xu, J., Franza, A., Marshall, A. M., & Losacco, N. (2021a). Role of footing embedment on tunnel–foundation interaction. *Journal of Geotechnical and Geoenvironmental Engineering, 147*(9), 06021009.

Xu, J., Franza, A., Marshall, A. M., Losacco, N., & Boldini, D. (2021b). Tunnel–framed building interaction: Comparison between raft and separate footing foundations. *Géotechnique, 71*(7), 631–644.

Xu, J., Gui, J., & Sheil, B. (2024). A numerical investigation of the role of basements on tunnel-frame interaction in sandy soil. *Computers and Geotechnics, 169*, 106197.

Yang, J., & Gu, X. Q. (2013). Shear stiffness of granular material at small strains: Does it depend on grain size? *Géotechnique, 63*(2), 165–179.

Yiu, W. N., Burd, H. J., & Martin, C. M. (2017). Finite-element modelling for the assessment of tunnel-induced damage to a masonry building. *Géotechnique, 67*(9), 780–794.

Zhang, X., Qin, H., Xu, Y., Qu, H., & Chen, C. (2024). Performance of an operational shield tunnel due to construction of a large cross-sectional straight-walled arch tunnel above-crossing. *Alexandria Engineering Journal, 108*, 863–877.